

A Heton Perspective of Baroclinic Eddy Transfer in Localized Open Ocean Convection

SONYA LEGG

Institute for Geophysics and Planetary Physics, University of California, Los Angeles, Los Angeles, California

HELEN JONES AND MARTIN VISBECK*

Department of Earth, Atmospheric and Planetary Sciences, Massachusetts Institute of Technology, Cambridge, Massachusetts

(Manuscript received 27 July 1995, in final form 4 April 1996)

ABSTRACT

A simple point-vortex "heton" model is used to study localized ocean convection. In particular, the statistically steady state that is established when lateral buoyancy transfer, effected by baroclinic instability, offsets the localized surface buoyancy loss is investigated. Properties of the steady state, such as the statistically steady density anomaly of the convection region, are predicted using the hypothesis of a balance between baroclinic eddy transfer and the localized surface buoyancy loss. These predictions compare favorably with the values obtained through numerical integration of the heton model.

The steady state of the heton model can be related to that in other convection scenarios considered in several recent studies by means of a generalized description of the localized convection. This leads to predictions of the equilibrium density anomalies in these scenarios, which concur with those obtained by other authors. Advantages of the heton model include its inviscid nature, emphasizing the independence of the fluxes affected by the baroclinic eddies from molecular processes, and its extreme economy, allowing a very large parameter space to be covered. This economy allows us to examine more complicated forcing scenarios: for example, forcing regions of varying shape. By increasing the ellipticity of the forcing region, the instability is modified by the shape and, as a result, no increase in lateral fluxes occurs despite the increased perimeter length.

The parameterization of convective mixing by a redistribution of potential vorticity, implicit in the heton model, is corroborated; the heton model equilibrium state has analogous quantitative scaling behavior to that in models or laboratory experiments that resolve the vertical motions. The simplified dynamics of the heton model therefore allows the adiabatic advection resulting from baroclinic instability to be examined in isolation from vertical mixing and diffusive processes. These results demonstrate the importance of baroclinic instability in controlling the properties of a water mass generated by localized ocean convection. A complete parameterization of this process must therefore account for the fluxes induced by horizontal variations in surface buoyancy loss and affected by baroclinic instability.

1. Introduction

A characteristic feature of open ocean deep convection is that it is highly localized, occurring in regions only a few tens of kilometers in diameter (Killworth 1983). As a result, horizontal density gradients are enhanced, promoting sheared baroclinic flow around the convecting "chimney" (Fig. 1). Many authors (i.e., Gascard 1978; Madec et al. 1991) have recognized that this rim current, if it becomes baroclinically unstable, must lead to lateral fluxes of fluid and buoyancy. Several recent studies of convection forced by a continued

surface buoyancy loss over a circular area, both in the laboratory (Brickman 1995; Ivey et al. 1995; Coates et al. 1995; Hufford et al. 1996, manuscript submitted to *J. Geophys. Res.*) and in numerical simulation (Send and Marshall 1995), have found that the lateral fluxes effected by the baroclinic instability may completely balance the surface fluxes. This results in a quasi-equilibrium state in which the density anomaly of the convected region is prevented from further increase. These studies have been of both convection into an initially homogeneous fluid and an initially stably stratified fluid. Visbeck et al. (1996a, hereafter VMJ) considered the properties of the equilibrium state in several of these studies and deduced scaling arguments for the equilibrium quantities based on a simple balance between the advective fluxes and surface forcing and employing a parameterization of these fluxes.

As an alternative to laboratory experiments and high-resolution numerical models, localized convection can be examined using the quasigeostrophic "heton"

* Current affiliation: Lamont-Doherty Earth Observatory, Columbia University, Palisades, New York.

Corresponding author address: Dr. Sonya Legg, Institute for Geophysics and Planetary Physics, UCLA, 405 Hilgard Ave., Los Angeles, CA 90095-1567.

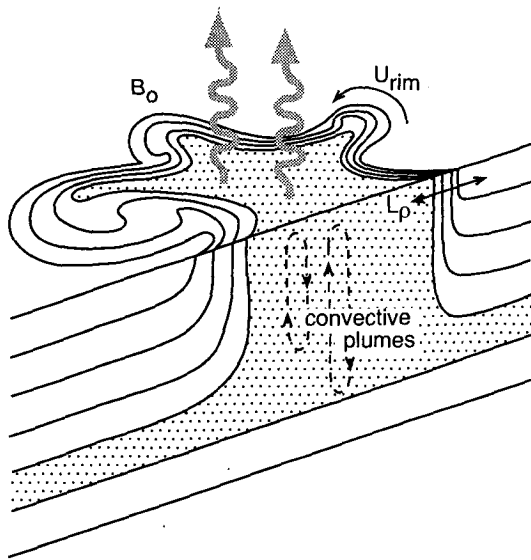


FIG. 1. A schematic diagram showing a section through a typical region of localized ocean convection, with solid lines representing isopycnal surfaces. Mixing by convective plumes initiated by a localized surface buoyancy loss B_0 generates a localized density anomaly (shaded region). Geostrophic adjustment leads to slumping on the scale of the deformation radius L_ρ , with an associated baroclinic rim current U_{rim} . Subsequent baroclinic instability generates eddies of the scale L_ρ .

model of Legg and Marshall (1993, hereafter LM). The heton model provides both a conceptually elegant parameterization of convection as a redistribution of potential vorticity and an economical tool for numerical integration of the buoyancy-forced circulation. LM demonstrated the existence of the equilibrium state in the heton model but did not attempt to investigate the parameter space dependence of this equilibrium state or to quantitatively relate the results with those of more complete numerical simulations or laboratory experiments of convection. Such a quantitative comparison is necessary to calibrate the model before it can be used to extend our understanding in more complicated regimes not yet tackled by other methods. Here we will derive the scaling arguments for the equilibrium state properties of the heton model using a generalized framework. This framework unifies three scenarios: convection into a homogeneous fluid, convection into a linearly stratified fluid, and convection represented in a two-layer model such as the heton model. A quantitative comparison of the heton model results with those of the other scenarios can therefore be made, and the heton model can be demonstrated to be a useful tool for investigating localized convection. The economy of the heton model provides a means of investigating more complex spatial and temporal patterns of forcing than can be readily accessed in the laboratory or more direct numerical simulations.

We begin in section 2 by reviewing features of an idealized baroclinically unstable chimney. In section 3 we then define and compare three conceptual models of the localized convecting region: the first appropriate to a two-layer quasigeostrophic numerical model such as the heton model (the two-layer model, Fig. 2a) and

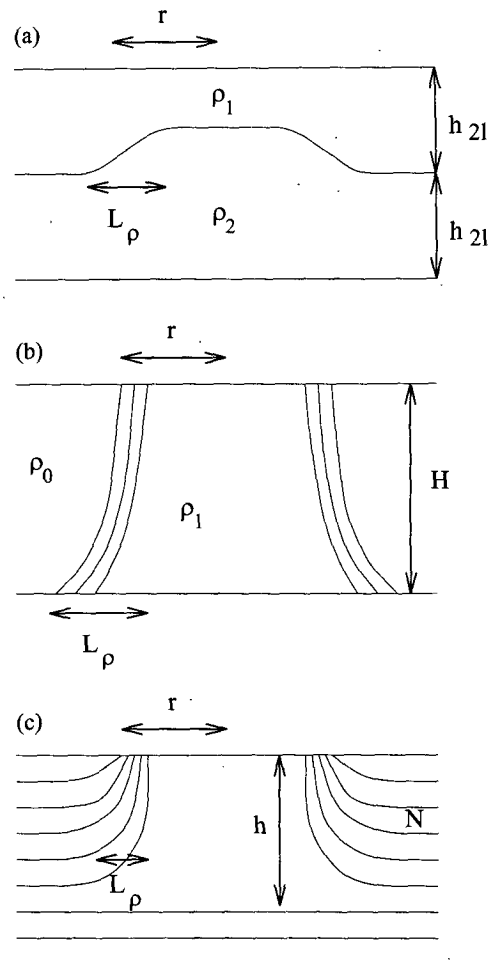


FIG. 2. Three possible convection scenarios when a surface buoyancy flux B_0 is applied over an area of radius r . (a) In a two-layer quasigeostrophic representation, buoyancy forcing raises the interface between the two layers, equivalent to a density anomaly. The deformation radius is given by $L_\rho = (1/\sqrt{2}f)[g(\rho_2 - \rho_1)h_{21}/\rho_0]^{1/2}$, where h_{21} is the layer depth, and ρ_1 and ρ_2 are the densities of the upper and lower layers, respectively. The equilibrium state is characterized by a constant density anomaly $\Delta\rho(eq)$. (b) In an initially homogeneous ocean, of density ρ_0 and depth H , convection penetrates to the bottom, generating a chimney of dense water of density $\rho_1 = \rho_0 + \Delta\rho$. This chimney of dense water relaxes to a state of geostrophic adjustment characterized by a deformation radius $L_\rho \sim (1/f)(gH\Delta\rho/\rho_0)^{1/2}$. The equilibrium state is characterized by a constant density anomaly $\Delta\rho(eq)$. (c) In an ocean of initial stable stratification N , convection mixes fluid to a depth h , given in the absence of lateral transport of fluid by $h = (2B_0t/N^2)^{1/2}$. The chimney of mixed fluid relaxes to a state of geostrophic adjustment characterized by a deformation radius $L_\rho \sim Nh/f$. The equilibrium state is characterized by a maximum mixed layer depth h_{max} .

the other two appropriate to the most common laboratory and numerical scenarios adopted in similar studies by other authors, one for convection into an initially unstratified fluid (the neutral model, Fig. 2b) and the other relevant to convection into an initially uniform stable stratification (the stratified model, Fig. 2c).

Section 4 provides a brief description of the heton model. Results from simulations performed to corroborate the two-layer predictions are given in section 5. In section 6 we consider variations in the shape of the forcing. Finally we include a discussion of the implications of the study.

2. Baroclinic instability and ocean convection

In oceanic convection, deep vertical mixing, localized through interactions between large-scale forcing and details of the circulation, generates a "chimney" of dense fluid (Fig. 1). In order to examine the influence of baroclinic instability on this chimney region, we shall assume it is unnecessary to understand the small-scale dynamics of individual plumes. This approach to the integral properties of convection has been proposed by Send and Marshall (1995), who argue chimney-scale properties depend only on the mixing effected by the plume ensemble as a whole.

Buoyancy loss at the chimney site results in an overall change in density there, the pool of denser water relaxing under gravity to a state of thermal wind balance so that the edge of the chimney slumps by a horizontal distance on the order of L_ρ , the deformation radius, and a baroclinic current U_{rim} is established around the periphery. This rim current may be baroclinically unstable, the instability growing at a rate determined by the ambient stratification, rim current velocity, and rotation rate (Coates et al. 1995). Numerical simulations and laboratory experiments have shown that, if surface forcing persists, baroclinic instability of the convecting chimney may lead to the establishment of a dynamic equilibrium in which the generation of a density anomaly through the surface forcing balances the flux of dense fluid out of the forced region.

a. Chimney-scale properties

A number of authors have proposed scalings for the properties of chimneys (Jones and Marshall 1993; Maxworthy and Narimousa 1994; Send and Marshall 1995), but no consensus has yet been reached. By way of review we outline here what is perhaps the simplest form of these scaling arguments, following closely the approach of Send and Marshall (1995) and VMJ in particular.

All three of our convection scenarios are governed by the equation for the rate of change of the density anomaly $\Delta\rho$ of the convecting region (assuming incompressibility and buoyancy conservation):

$$\frac{d}{dt} \int_{A_1, h} \Delta\rho dV = \frac{\partial}{\partial t} \int_{A_1, h} \Delta\rho dV + \oint_S \mathbf{J} \cdot d\mathbf{S} = \int_{A_1} \frac{B_0 \rho_0}{g} dA, \quad (1)$$

where, with reference to Fig. 3, the integral on the left-hand side is carried out over a volume, defined by the depth of convecting fluid h and the surface area A_1 , undergoing buoyancy loss and the surface integral on the right-hand side is carried out over area A_1 . Here ρ_0 is a reference density, B_0 is the applied surface buoyancy flux, g is the gravitational acceleration, and d/dt is the full derivative, involving the time rate of change within the volume considered, the time rate of change of the volume itself (due to convective deepening), and fluxes out of that volume; \mathbf{J} is the density flux out of the volume and $d\mathbf{S}$ is the vector normal to the surface S bounding the volume.

The dense water chimney adjusts under gravity, slumping over a distance comparable with the deformation radius

$$L_\rho \sim \frac{1}{f} \left(\frac{g \Delta\rho}{\rho_0} h \right)^{1/2}, \quad (2)$$

where f is the Coriolis parameter.

A baroclinic rim current is generated through geostrophic adjustment satisfying the thermal wind equation:

$$\frac{\partial u}{\partial z} = \frac{g}{f \rho_0} \frac{\partial \rho}{\partial y}, \quad (3)$$

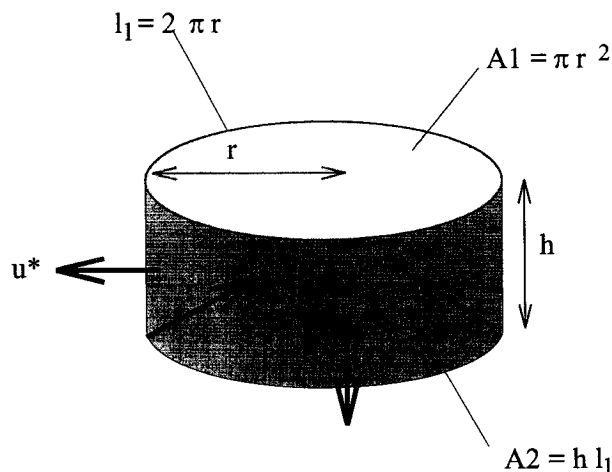


FIG. 3. A schematic diagram showing the fluxes of anomalous density out of the volume, and generation of density anomaly within the volume, defined by the depth of the convective region h , and the area affected by the surface forcing $A_1 = \pi r^2$. The density difference between the convected volume and surrounding fluid is $\Delta\rho$, while u^* is the effective root-mean-square flux velocity across the bounding surface of area $A_2 = h l_1$.

and we estimate the magnitude of this baroclinic rim current, U_{rim} :

$$U_{\text{rim}} \sim \frac{gh}{f\rho_0} \frac{\Delta\rho}{L_p}. \quad (4)$$

b. A quasi-equilibrium state

Baroclinic instability of the rim current may lead to the establishment of a quasi-equilibrium state. In all three scenarios this quasi-equilibrium is characterized by a constant density anomaly within the chimney region (Send and Marshall 1995; Brickman 1995; Legg and Marshall 1993); however, in the case of convection into an initially stably stratified fluid, the constant density anomaly is associated with an equilibrium mixed layer depth (Ivey et al. 1995; Coates et al. 1995; VMJ). In each case, the density changes induced by the surface forcing are exactly balanced by the flux of density out of the chimney region by the baroclinic instability.

We write the flux of anomalous density out of the forcing region as $\mathbf{J} = \langle u_r \rho' \rangle \mathbf{n} = u^* \Delta\rho \mathbf{n}$, where u_r is the velocity perturbation in the radial direction, ρ' is the density perturbation, \mathbf{n} is the unit vector normal to the bounding surface, and the brackets imply the mean over the surface area bounding the forcing region; u^* is a root-mean-square velocity fluctuation in the direction of \mathbf{n} . Implicit in this formalism is the assumption of no net mean flow when integrated in the vertical direction and an axisymmetric basic state. This implies no background zonal or meridional shear. However, axisymmetric mean flow (which must from continuity integrate to zero in the vertical) is not excluded. Such a flow has a root-mean-square variation compared to the zero mean vertically integrated flow, which will be included above.

Then we can express the statement of balance between generation and removal of anomalous density, when $\partial\Delta\rho/\partial t = 0$ within the volume considered and the volume remains constant, as

$$\int_{A_1} \frac{B_0 \rho_0}{g} dA = \int_h \oint_{l_1} u^* \Delta\rho dl dz, \quad (5)$$

where l_1 is the chimney's circumference ($l_1 = 2\pi r$ if forcing is in the form of a circular disc of radius r) (Fig. 3).

Apart from the quantity we wish to deduce, the equilibrium density anomaly or corresponding mixed layer depth, the only unknown is u^* , the root-mean-square velocity of fluid out of the patch. If we can parameterize u^* in terms of the mean chimney properties, we will be able to predict the equilibrium state in which this balance of fluxes applies.

Following the arguments of Stone (1972), we use a linear stability approach to estimate u^* , given an instability growing at the rate given by Eady (1949), with

the length scale of the fastest-growing mode. This leads to an estimate of u^* proportional to the rim current velocity

$$u^* = \alpha U_{\text{rim}}, \quad (6)$$

where α is a constant of proportionality to be determined.

Since U_{rim} is independent of f [Eqs. (4) and (2)], u^* must itself be independent of f . Note that this relationship between u^* and U_{rim} can be obtained from energetic arguments (VMJ). If we now substitute for u^* from Eqs. (6) and (4) into Eq. (5) and integrate over the specified volumes and areas, a prediction for the equilibrium density anomaly is obtained:

$$\left(\frac{g}{\rho_0} \Delta\rho_{\text{eq}} \right)^4 = \frac{g}{\rho_0} \Delta\rho_L \frac{(B_0 r)^2}{4\alpha^2 h^3}, \quad (7)$$

where ρ_L is the density difference used to define $L_p = \sqrt{(g\Delta\rho_L h/\rho_0)}/f$. A key difference between the quasigeostrophic model and the other scenarios is that $\Delta\rho_L \neq \Delta\rho_{\text{eq}}$ in the quasigeostrophic formulation. Note that (7) does not include any dependence on rotation, a property arising through the independence of u^* from f .

In addition to $\Delta\rho_{\text{eq}}$ a second key parameter is the time taken for equilibrium to become established, T_{eq} , since this will dictate whether convection is essentially vertical (closely obeying one-dimensional mixing physics) or is sufficiently long-lived to be in this, more unconventional, laterally advective limit. A lower limit for the equilibrium timescale is the time at which $\Delta\rho(t) = \Delta\rho_{\text{eq}}$, assuming one-dimensional mixing physics, since it must take at least as long as this to achieve a depth h_{max} or equivalent density $\Delta\rho_{\text{eq}}$. Then, given the linear relationship between $\Delta\rho$ and t in the absence of lateral fluxes, we have

$$T_{\text{eq}} \geq \Delta\rho_{\text{eq}} / (d\Delta\rho/dt). \quad (8)$$

Given flux balance is achieved through chimney disintegration, we shall further assume the time it takes the patch to break up T_b to be proportional to T_{eq} . Note that implicit in this estimate is the assumption that the timescale for baroclinic instability is less than T_{eq} , since it is the development of the baroclinic instability that allows the equilibrium to be achieved. We predict from (8) that T_b is, like $\Delta\rho_{\text{eq}}$, independent of rotation.

3. Three ocean convection models

We now explicitly derive these equilibrium quantities in the three different conceptual models chosen to represent typical localized convection scenarios. The first describes the two-layer quasigeostrophic idealization examined numerically using the heton model by LM, while the other two correspond to previously published laboratory and numerical studies. The relevant quantities are summarized in Table 1. In all three cases

we assume that forcing takes the form of a circular disc of radius r ; a later section will describe modifications expected for alternative shapes of forcing.

The essential differences between the three scenarios are (i) the depth over which the buoyancy forcing is acting, corresponding to the depth of the convective layer h , and (ii) the density difference $\Delta\rho_L$, which determines the deformation radius L_ρ . These differences make it necessary to derive the appropriate quantities separately for each scenario. Quasigeostrophic results in particular cannot be applied to the real ocean without an appreciation of the differences introduced by assuming small density perturbations. Nevertheless, we will show that the mechanisms described above apply in all three cases, leading to analogous scaling of the equilibrium density anomaly.

In order to facilitate the comparison between the equilibrium quantities in the different scenarios, we will make use of the important nondimensional parameters identified by VMJ for this localized convection problem:

$$\text{Ro}^* = \left(\frac{B_0}{f^3 H^2} \right)^{1/2} ; \frac{r}{H} ; \frac{N}{f}. \quad (9)$$

Here Ro^* is the natural Rossby number of Fernando et al. (1991), Jones and Marshall (1993), and Maxworthy and Narimousa (1994) and provides a measure of the forcing timescale as compared to the rotational timescale; r/H is a measure of the geometry of the forcing region; and N/f is the ratio of Brunt–Väisälä to inertial frequencies. Typical oceanic values of Ro^* may be close to or less than unity, in deep convection regions, while $r/H \gg 1$ and N/f may vary significantly from region to region. Combining Ro^* and r/H gives another useful parameter: the ratio of the horizontal length scale of the forcing region to the rotational length scale $l_{\text{rot}} = (B_0/f^3)^{1/2}$ proposed by the above authors as the scale at which rotation influences convection:

$$\frac{r}{H \text{Ro}^*} = \frac{r}{l_{\text{rot}}}. \quad (10)$$

Typically r/l_{rot} is of the order $50 \rightarrow 100$. We will see that all interesting quantities can be expressed in terms of these nondimensional parameters in all three convection scenarios.

a. Buoyancy loss in a two-layer quasigeostrophic model: Two-layer scenario

In a two-layer representation of a buoyancy anomaly (Fig. 2a), the only possible depth scale is the layer thickness $h_{2l} = H/2$, over which the forcing applies. In this representation the stratification is defined by $N^2 = g \Delta\rho_{1,2}/(\rho_0 h_{2l})$, where $\Delta\rho_{1,2}$ is the density difference between the layers. The effect of buoyancy loss is to raise the interface between the layers by an amount η

so that some formerly upper-layer fluid has changed its density to that of the lower layer. Hence, a density anomaly $\Delta\rho = \eta \Delta\rho_{1,2}/(2h_{2l})$ results.

The deformation radius is determined by the initial stratification and the layer thickness, defined in the equations of motion (see appendix) as

$$L_\rho = \frac{N h_{2l}}{\sqrt{2} f}; \quad (11)$$

that is, $\Delta\rho_L = \Delta\rho_{1,2}/2$. Here L_ρ is constant with time in contrast with the $t^{1/2}$ dependence of the neutral and stratified models we shall consider, a direct consequence of the quasigeostrophic assumption that density perturbations may be considered “small” (see, for example, Charney 1947).

Hence from Eq. (7) the equilibrium density anomaly is given by

$$\Delta\rho_{\text{eq}} = \frac{1}{2^{1/4} (2\alpha)^{1/2}} \frac{\rho_0}{g} \left(\frac{N B_0 r}{h_{2l}} \right)^{1/2} \sim \frac{\rho_0 f^2 h_{2l}}{g} \left(\frac{N}{f} \frac{r}{h_{2l}} \text{Ro}^{*2} \right)^{1/2}, \quad (12)$$

where Ro^* is expressed in terms of the layer depth h_{2l} . We expect equilibrium to be reached in a time

$$T_b \sim \frac{\Delta\rho_{\text{eq}}}{d\Delta\rho/dt} \sim \left(\frac{r N h_{2l}}{B_0} \right)^{1/2} \sim \frac{1}{f} \left(\frac{N}{f} \frac{r}{h_{2l}} \frac{1}{\text{Ro}^{*2}} \right)^{1/2}. \quad (13)$$

Numerical verification of these results is the focus of later sections of this paper.

b. Convection into a neutral ocean: Neutral model

In this model there is no background density stratification to obstruct deepening so that the chimney rapidly extends to the ocean floor, such that $h = H$, the total ocean depth (Fig. 2b). In the absence of lateral buoyancy fluxes

$$\Delta\rho = \frac{B_0 \rho_0 t}{g H}; \quad L_\rho \sim \frac{\sqrt{B_0 t}}{f}, \quad U_{\text{rim}} \sim \sqrt{B_0 t} \quad (14)$$

as in Send and Marshall (1995). Note that unlike the two-layer model, where L_ρ is constant and U_{rim} proportional to t , both are here proportional to $t^{1/2}$ and $\Delta\rho_L = \Delta\rho$.

Baroclinic instability leads to fluxes of dense fluid out of the cooling region (Fig. 4), and the development of an equilibrium state characterized by a constant density anomaly. Substituting for h and $\Delta\rho_L$ in (7) to obtain a relationship for $\Delta\rho_{\text{eq}}$, the equilibrium density anomaly is

$$\Delta\rho_{\text{eq}} = \frac{1}{(2\alpha)^{2/3}} \frac{\rho_0}{g H} (B_0 r)^{2/3} \sim \frac{\rho_0 f^2 H}{g} \left(\text{Ro}^{*2} \frac{r}{H} \right)^{2/3}, \quad (15)$$

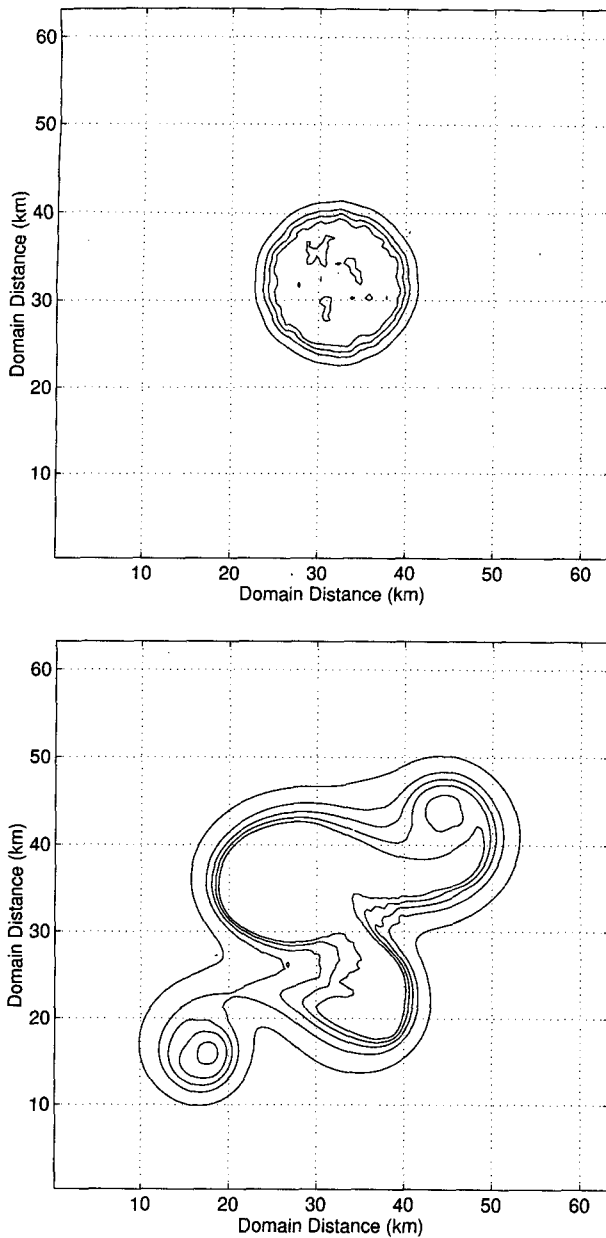


FIG. 4. A horizontal section showing the structure of the density anomaly (a) 1 day after the onset of cooling and (b) 10 days after the onset of cooling, before and after the onset of baroclinic instability, respectively, in the neutral model [calculated using the numerical model described in Jones and Marshall (1993)]. The surface forcing is confined to a disc of diameter 16 km in the center of the domain. The contour interval is 0.001 kg m^{-3} .

and the breakup time is

$$T_b \sim \frac{\Delta \rho_{\text{eq}}}{d\Delta \rho/dt} \sim \left(\frac{r^2}{B_0}\right)^{1/3} \sim \frac{1}{f} \left(\frac{r}{l_{\text{rot}}}\right)^{2/3}. \quad (16)$$

These results have previously been obtained by VMJ and have been verified in the laboratory by Brickman

(1995) and Narimousa (1996, manuscript submitted to *J. Geophys. Res.*).

Although the two-layer model's quasigeostrophy introduces differences in time dependence when compared with this model, features of the steady state are similar: the equilibrium density anomaly (15) can be obtained from Eq. (12) by replacing N^2 with $2g\Delta\rho_{\text{eq}}/(\rho_0 H)$.

c. Convection into a stratified ocean: Stratified model

In the final convection model we consider, a preexisting density stratification must be eroded to achieve chimney deepening. When convection occurs to disrupt a stable, horizontally homogeneous density profile (Fig. 2c), then the average density anomaly of the mixed layer

$$|\Delta\rho| = \frac{\rho_0}{g} \frac{N^2 h}{2}, \quad (17)$$

where $N^2 = -(g/\rho_0)(\partial\rho/\partial z)$ is the square of the Brunt–Väisälä frequency and h is now the time-dependent mixed layer depth:

$$h = \left(\frac{2B_0 t}{N^2}\right)^{1/2} \quad (18)$$

(Turner 1973). This presumes no turbulent entrainment at the mixed layer base and that the sole effect of convection is to mix the water column to a state of neutral static stability.

The relevant chimney-scale quantities, obtained by substituting Eq. (17) in Eqs. (2) and (4), are

$$L_p \sim \frac{Nh}{f}, \quad U_{\text{rim}} \sim Nh; \quad (19)$$

that is, $\Delta\rho_L = \Delta\rho$.

Given (18), the time dependence of L_p and U_{rim} in the neutral and stratified models is the same.

Substituting for $\Delta\rho_L$ and $\Delta\rho$ in (7) in terms of h ,

$$h_{\text{max}} = \frac{2^{1/2}}{(2\alpha)^{1/3}} \frac{(B_0 r)^{1/3}}{N} \sim H \left(\text{Ro}^* \frac{r}{H} \right)^{1/3} \left(\frac{f}{N} \right), \quad (20)$$

implying from (17) that

$$\Delta\rho_{\text{eq}} = \frac{1}{2^{1/2}(2\alpha)^{1/3}} \frac{\rho_0 N}{g} (B_0 r)^{1/3} \quad (21)$$

and

$$T_b \sim \frac{h_{\text{max}}}{dh/dt} \sim \left(\frac{r^2}{B_0}\right)^{1/3} \sim \frac{1}{f} \left(\frac{r}{l_{\text{rot}}}\right)^{2/3} \quad (22)$$

as for the neutral model and obtained and verified by VMJ.

Here h_{max} and $\Delta\rho_{\text{eq}}$ are, like $\Delta\rho_{\text{eq}}$ in the neutral model, independent of f and can be deduced from the

neutral model result by replacing H by h_{\max} . Similarly h_{\max} can be deduced from Eq. (12) if $\Delta\rho_{\text{eq}}$ is replaced by $N^2\rho_0 h_{\max}/(2g)$ and h_{2l} with h_{\max} .

d. Comparison of numerical values

Introducing appropriate constants of proportionality, the following equalities pertain at equilibrium

$$\Delta\rho_{\text{eq}}(\text{neutral model}) = \gamma_n \frac{\rho_0}{gH} (B_0 r)^{2/3} \quad (23)$$

$$h_{\max}(\text{stratified model}) = \gamma_s \frac{(B_0 r)^{1/3}}{N} \quad (24)$$

$$\Delta\rho_{\text{eq}}(\text{two-layer model}) = \gamma_{2l} \frac{\rho_0}{g} \left(\frac{NB_0 r}{h_{2l}} \right)^{1/2}, \quad (25)$$

where γ_n , γ_s , and γ_{2l} are numerical constants.

All the numerical constants depend only on the closure parameter α , the constant of proportionality relating the effective flux velocity u^* to the rim current velocity:

$$\gamma_n = \frac{1}{(2\alpha)^{2/3}}; \quad \gamma_s = \frac{2^{1/2}}{(2\alpha)^{1/3}}; \quad \gamma_{2l} = \frac{1}{(2\alpha)^{1/2} 2^{1/4}}. \quad (26)$$

Hence α can be determined by evaluating γ_{2l} :

$$\alpha = \frac{1}{2^{3/2} \gamma_{2l}^2}. \quad (27)$$

For future reference, this information is summarized in Table 1. Note that VMJ obtained $\gamma_s = 3.9$ from examination of several numerical and laboratory studies.

4. The heton model

Before testing our two-layer predictions we begin with a description of the heton model, which is a par-

ticular numerical implementation of the two-layer quasigeostrophic model. We wish to model the evolution of the density anomaly of the convected region, and associated baroclinic flow, with nonlinear dynamics, at low resolution, in order to study as large a parameter space as possible, but without the usual accompanying problem of high diffusivities. Furthermore, since the equilibrium state involves lateral fluxes of fluid to large distances, we do not wish to be restricted in our domain size. A Lagrangian inviscid model with an unbounded domain will allow us to achieve these aims but is not possible without some discretization of the anomaly. The discretization we choose is the heton model of Hogg and Stommel (1985), details of which are given in LM. A two-layer discretization is used in the vertical, the simplest possible representation of the baroclinic structure of the chimney. A point vortex discretization is used in the horizontal, which has the advantage over other available discretizations (e.g., contour dynamics) of allowing a controllable element of randomness and spatial variability in the density anomaly, mimicking the local variations in surface buoyancy flux. Variations in the shape and distribution of the forcing can also be readily incorporated.

The two-layer model is formulated in terms of quasigeostrophic potential vorticity, which includes both velocity field and density anomaly information. (For details of the model equations, see the appendix.) The potential vorticity anomaly is related to the density anomaly of the region through

$$q = \frac{gf}{\rho_0 N^2 h_{2l}} \Delta\rho, \quad (28)$$

where q is the baroclinic component of the potential vorticity anomaly. In the two-layer discretization of equal layer depths, the potential vorticity anomalies in each layer are given by $q_1 = q$, $q_2 = -q$. As described in LM, we have parameterized the effect of convection by a redistribution of potential vorticity within the wa-

TABLE 1. Summary of parameters for the three scenarios.

	Neutral scenario	Stratified scenario	Two-layer scenario
Depth scale	H	h	h_{2l}
Rossby radius	$L_\rho \sim \frac{1}{f} \left(\frac{g\Delta\rho H}{\rho_0} \right)^{1/2}$	$L_\rho \sim \frac{Nh}{f}$	$L_\rho = \frac{Nh_{2l}}{\sqrt{2}f}$
Rim current speed	$U_{\text{rim}} \sim \left(\frac{g\Delta\rho H}{\rho_0} \right)^{1/2}$	$U_{\text{rim}} \sim Nh$	$U_{\text{rim}} \sim \frac{g\Delta\rho}{\rho_0 N}$
Equilibrium value	$\Delta\rho = \gamma_n \frac{\rho_0}{gH} (B_0 r)^{2/3}$	$h_{\max} = \gamma_s \frac{(B_0 r)^{1/3}}{N}$	$\Delta\rho = \gamma_{2l} \frac{\rho_0}{g} \left(\frac{NB_0 r}{h_{2l}} \right)^{1/2}$
Coefficients	$\gamma_n = \frac{1}{(2\alpha)^{2/3}}$	$\gamma_s = \frac{2^{1/2}}{(2\alpha)^{1/3}}$	$\gamma_{2l} = \frac{1}{2^{1/4}(2\alpha)^{1/2}}$
Calculated values	$\gamma_n = 1.6 \pm 0.4$	$\gamma_s = 1.8 \pm 0.2$	$\gamma_{2l} = 1.2 \pm 0.2$

ter column, a concept currently being pursued in the development of parameterizations of convection for models that are continuous in the vertical (J. Marshall 1995, personal communication).

The baroclinic structure of the convected region is represented by an ensemble of baroclinic point vortex pairs of potential vorticity $\pm s\delta(r - r_i)$, where $\pm s$ is the strength of the point vortex in the upper and lower layer, respectively, each point vortex pair being termed a heton (Hogg and Stommel 1985). The point vortices also act as dynamical tracers, indicating by their movement the transport of convected fluid. The average potential vorticity anomaly \bar{q} over the convection region is related to the number of hetons there by

$$\int q dA = \bar{q}A = \mathcal{N}s, \quad (29)$$

where \mathcal{N} is the number of hetons and A is the area over which the average is evaluated. Substituting from Eq. (28) into Eq. (29), the number of hetons within a region is related to the average density anomaly of the region by

$$\mathcal{N} = \frac{A}{s} \frac{gf}{\rho_0 N^2 h_{2l}} \Delta\rho. \quad (30)$$

By examining the number of vortices and their flux, we can deduce the density anomaly and the lateral density flux.

As shown in the appendix, the behavior of a heton ensemble depends on three nondimensional parameters:

$$R_q = \frac{B_0}{h_{2l}^2 N^2 f} = \left(\frac{l_{\text{rot}}}{h_{2l}}\right)^2 \left(\frac{f}{N}\right)^2 = \frac{1}{2} \left(\frac{l_{\text{rot}}}{\lambda}\right)^2 = \text{Ro}^{*2} \left(\frac{f}{N}\right)^2 \quad (31)$$

$$\mu = \frac{r}{\lambda} = \frac{\sqrt{2}rf}{Nh_{2l}} = \sqrt{2} \frac{r}{h_{2l}} \frac{f}{N} \quad (32)$$

$$S_p = \frac{s}{\lambda^2 f}, \quad (33)$$

where $\lambda = Nh_{2l}/(\sqrt{2}f)$, a modified deformation radius and $l_{\text{rot}} = (B_0/f^3)^{1/2}$.

Here R_q can be considered a form of Rossby number since it is the ratio between the potential vorticity anomaly generated in a time $1/f$ compared to the planetary vorticity f . Typical parameters associated with ocean convection give a value of $R_q \ll 1$ so that the quasigeostrophic assumption is valid.

In (32) μ is the ratio of the radius over which cooling is occurring compared to the deformation radius λ . The smallness of the deformation radius in the ocean means that convecting regions usually have $\mu > 1$ and so are baroclinically unstable (Pedlosky 1985).

In (33) S_p is the area associated with each vortex when the average potential vorticity of the patch $q = f$,

nondimensionalized by λ^2 . It is a measure of the sparseness of the point vortices and is an indicator of the degree to which the potential vorticity has been discretized. Experiments performed in LM demonstrated that the physical properties of the chimney show no dependence on S_p , provided it is sufficiently small that point vortices are close enough to interact as an ensemble. Here S_p is simply an artifact of the point-vortex discretization and would be a matter for concern if it did, in fact, influence the large-scale dynamics.

Note that while μ and R_q can be expressed in terms of the nondimensional parameters previously described, instead of having three physical nondimensional parameters we now have only two (since S_p refers to the model formulation rather than the physics of the problem). This reflects the loss of a degree of freedom, a result of the quasigeostrophic constraint that $L\rho$ is no longer a freely evolving parameter but is instead a constant of the model.

We can rewrite the equilibrium number of hetons in the chimney region, \mathcal{N}_{in} , in terms of the nondimensional parameters, by relating \mathcal{N}_{in} to $\Delta\rho_{\text{eq}}$, Eq. (25), through Eq. (30), as

$$\mathcal{N}_{\text{in}}(\text{eq}) = \frac{\lambda_{2l} 2^{-1/4} \pi \mu^2}{S_p} \sqrt{R_q \mu} = \gamma_x \mu^2 \sqrt{R_q \mu}, \quad (34)$$

where the numerical constant $\gamma_x = \gamma_{2l} \pi 2^{-1/4} / S_p$.

The breakup time, Eq. (13), can similarly be expressed in terms of the nondimensional parameters of the model:

$$T_b \sim \frac{1}{f} \left(\frac{\mu}{R_q}\right)^{1/2}. \quad (35)$$

Equations (34) and (35) allow us to compare the results of heton model integrations with the predictions for the three different scenarios in a straightforward manner.

The dependence of the equilibrium properties on R_q and μ are considered in the numerical integrations described below.

5. Results of the heton model for circular geometry

In LM, a ‘‘reference experiment’’ was performed with values of nondimensional parameters, $R_q = 0.08$, $\mu = 5.0$, $S_p = 1.9$. The hetons were introduced at a constant rate given by Eq. (A.3b) into the disc of radius $\mu\lambda$. The initial coordinates of each vortex were randomly chosen, but with a minimum separation 0.5λ from any other preexisting vortex. As the ensemble of baroclinic vortices builds, a large-scale baroclinic circulation develops around the edge of the chimney, which after a time $15/f$ develops a mode number 4 instability. The finite-amplitude development of the instability leads to heton clusters of radius about λ , breaking out of the forcing region. The clusters are tilted in the vertical so as to form self-propagating dipoles,

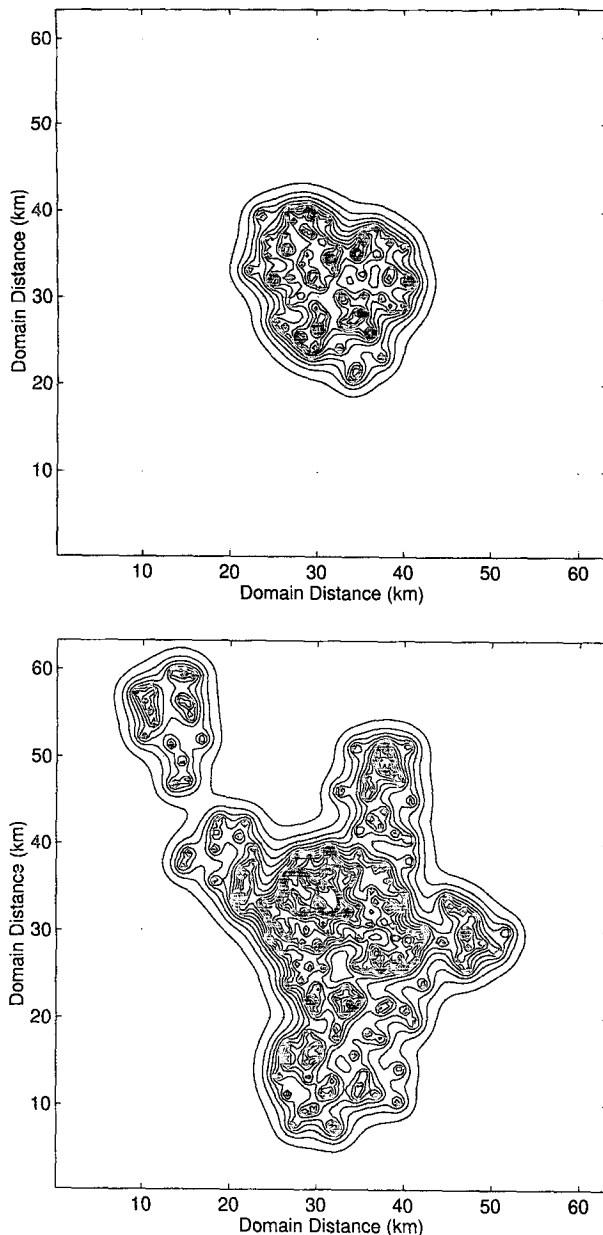


FIG. 5. The structure of the density anomaly (a) 1 day after the onset of cooling and (b) 3 days after the onset of cooling, before and after the onset of baroclinic instability, respectively, in the two-layer model reference experiment. The contour interval is 0.001 kg m^{-3} . Note the general similarity in shape between this anomaly and that shown in Fig. 4, with lobes of dense fluid moving away from the convection region of diameter 16 km in the center of the integration domain.

which flux dense fluid out of the chimney (Fig. 5) and thereby provide a lateral buoyancy flux inward. This behavior has been noted in several other studies of the baroclinic breakup of a circular density anomaly (for example, Griffiths and Hopfinger 1984; Helfrich and Send 1988) and is also seen in the other convection

scenarios (Fig. 4). An equilibrium is established in which the flux of hetons out of the patch due to baroclinic instability is equal to the rate at which they are generated by the buoyancy forcing (Fig. 6) and the lateral buoyancy flux is therefore sufficient to completely balance the surface buoyancy loss.

In the present study we performed two series of integrations of the heton model, the first at constant $\mu = 5.0$, varying R_q , and the second at constant $R_q = 0.08$, with varying μ (see Fig. 7), in all cases integrating until the properties of the equilibrium state could be determined. A total of 36 numerical integrations was performed for each series described. Such a large number was necessary in order to reduce the uncertainty with which the scaling exponents could be deduced. Currently such a series would not be economically feasible using a fully three-dimensional numerical model. Integration of the nonhydrostatic model of Jones and Marshall (1993) on a $132 \times 132 \times 20$ grid, carrying five variables, with a time step of 60 s for a period of 4 days, for example, involves a conservative 10^{12} floating point operation (flops) and requires 35 million bytes of memory. The heton model, when run with $R_q = 0.08$ and $\mu = 5.0$ for a similar time, requires a maximum of 0.8 million bytes while performing a total of only 4.9×10^9 flops.

A convenient nondimensional parameter by which to compare different studies of localized convection is $r/l_{\text{rot}} = r(f^3/B_0)^{1/2} = \mu/(2R_q)^{1/2}$ because it is based

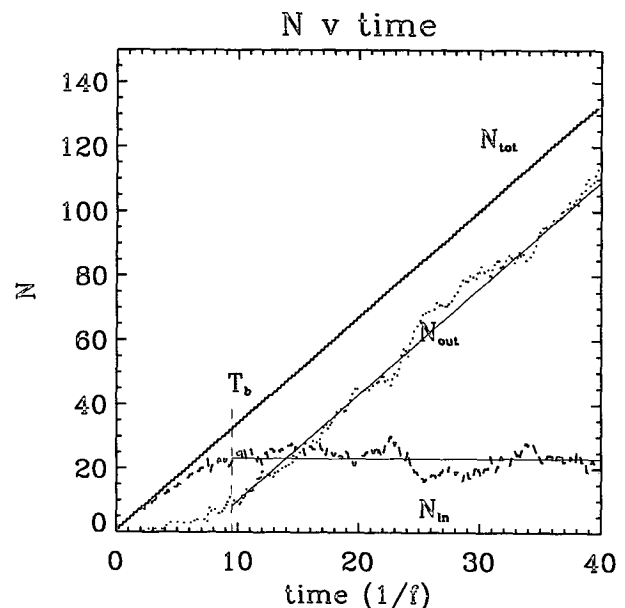


FIG. 6. The evolution of the heton numbers in the reference experiment: N_{tot} is the total number of hetons generated at a constant rate; N_{in} is the number of hetons within the chimney region of radius μ ; N_{out} is the number of hetons outside of this region. Also shown are $T_b f$ (dashed line) and $N_{\text{in}}(\text{eq})$ calculated from these results and the corresponding steady state N_{out} (thin solid lines).

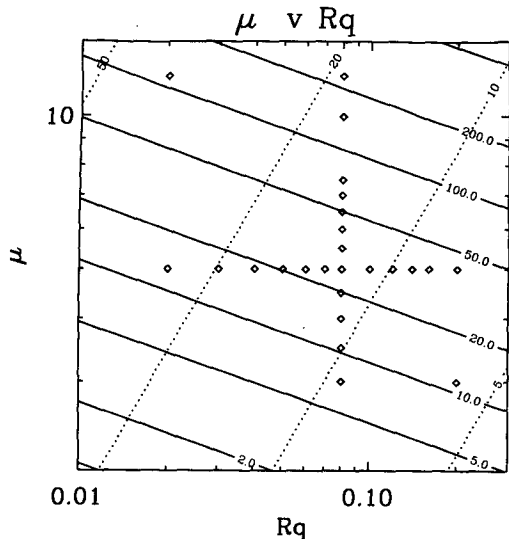


FIG. 7. The parameter space in R_q and μ covered in the heiton experiments (diamonds). Also shown are the predicted values of T_{bf} (dotted lines) and $\mathcal{N}_{in}(eq)$ (solid lines), making use of the numerical constants deduced through examination of the results in section 6c.

solely on external parameters in all three scenarios. The values of r/l_{rot} covered by the heiton model are compared to those investigated by other researchers in Fig. 8. The high density of results obtained for the larger, more physically interesting values of r/l_{rot} in addition to the large range of values covered attest to the economy of the heiton model.

a. The dependence of the final properties on R_q

A series of experiments was performed keeping μ and S_p constant at 5.0 and 1.9, respectively, and varying R_q . All experiments displayed the same qualitative behavior with the generation of a baroclinic rim current around the region of surface buoyancy forcing, the growth of a mode 4 instability, and the breakup of the convected patch into self-propagated tilted heiton clusters, leading to an equilibrium state in which the numbers of hetons within the chimney remain approximately constant.

We use the time at which the rate of change of hetons outside the patch (averaged over 20 time steps to eliminate small fluctuations) is equal to the total rate of change of hetons as a measure of the breakup time, T_b , since after this time the number of hetons within the patch ceases to increase further and breakup has therefore been established (see Fig. 6). The equilibrium number of hetons in the chimney $\mathcal{N}_{in}(eq)$ is calculated as the time-mean number of hetons in the patch after the breakup. Shown in Fig. 9 is the nondimensionalized breakup time $T_b f$ plotted against R_q in log-log form. The large estimated uncertainty does not allow us to distinguish whether $T_b f$ follows the predicted $R_q^{-1/2}$

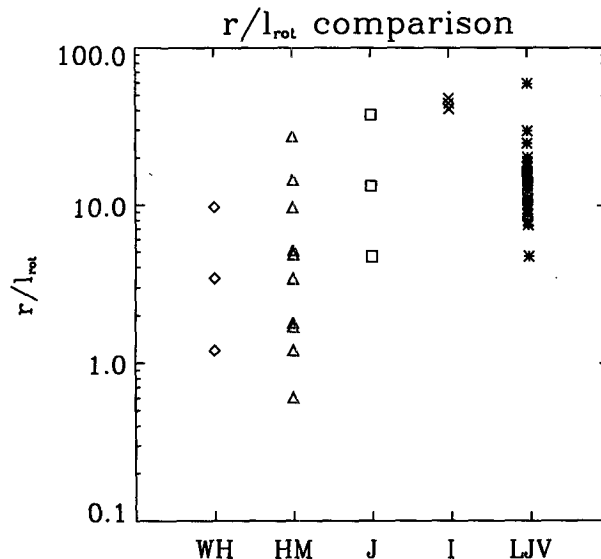


FIG. 8. A comparison of r/l_{rot} parameter space covered in the heiton experiments, compared to other researchers. Shown are the laboratory experiments of Whitehead and Hufford (WH), numerical simulations of Hufford and Marshall (HM), numerical simulations of Jones (J), laboratory experiments of Ivey et al. (I), and the heiton experiments described in this paper (LJV).

scaling behavior or is, in fact, independent of R_q . Nonetheless, Eq. (35) is not refuted by these results. Figure 10, showing \mathcal{N}_{in} plotted against R_q , demonstrates the predicted scaling behavior: $\mathcal{N}_{in}(eq) \propto R_q^{1/2}$, Eq. (34),

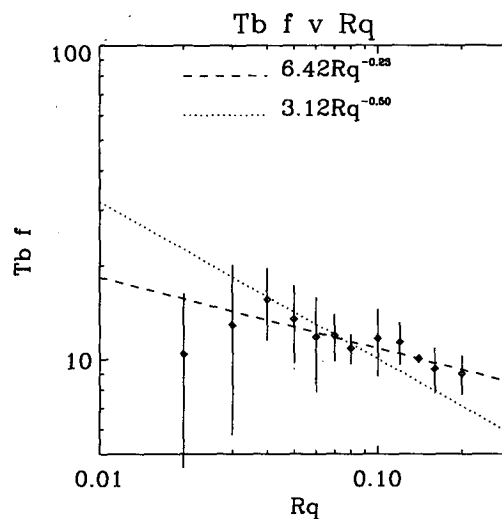


FIG. 9. Plot of $T_b f$ vs R_q at constant μ . Shown are the data points and the best fit to these data points $T_b f = A1 R_q^n$, where $A1$ and n are found empirically to equal 6.42 and -0.23 , respectively. The estimated error in the calculation of n is ± 0.22 , and this value is therefore within two standard deviations of the predicted value $n = -0.5$. Also shown is the best fit of $T_b f = A2 R_q^{-1/2}$ to the data, where $A2 = 3.18$. As in the next three figures, each point shown is the mean of results taken from three individual numerical integrations.

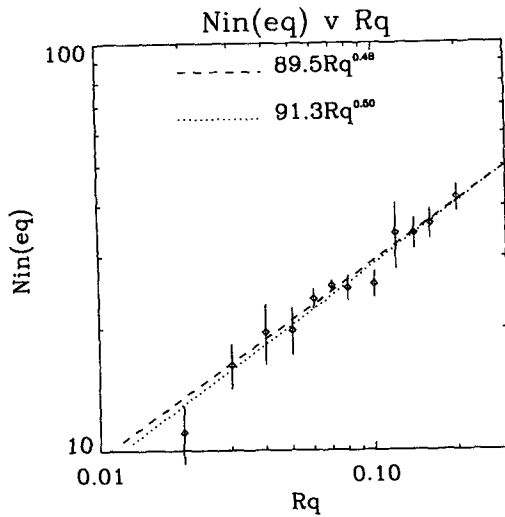


FIG. 10. Plot of \mathcal{N}_{in} vs R_q at constant μ . Shown are the data points, the best fit to these data points $\mathcal{N}_{in} = A1R_q^n$, and the best fit of $\mathcal{N}_{in} = A2R_q^{1/2}$ to the data. $A1 = 89.45$, $n = 0.48 \pm 0.11$, and $A2 = 91.3 \pm 6.1$. Term n therefore lies within one standard deviation of the predicted value.

to within estimated uncertainty. The constants of proportionality will be considered in a later section.

b. Dependence of properties on μ

A second series of experiments was performed, keeping R_q and S_p fixed at 0.08 and 1.9 respectively, and varying the radius of the cooling region μ . As before, the generation of a baroclinic rim current leads to the development of an instability, now with mode number varying in proportion to the patch radius, and eventually an equilibrium state is reached. In Fig. 11, the breakup time T_{bf} is shown plotted in log-log form against μ , showing that the approximate scaling behavior $T_{bf} \propto \sqrt{\mu}$ is obtained. In Fig. 12, the equilibrium number of hetons in the patch \mathcal{N}_{in} is shown plotted in log-log form against μ , demonstrating that the approximate relationship $\mathcal{N}_{in} \propto \mu^{5/2}$ exists. We have therefore verified that at constant S_p , Eqs. (34) and (35) correctly predict the behavior of the dense fluid patch in the heton model. To verify these results further we performed two additional sets of experiments, at $R_q = 0.2$, $\mu = 3.0$, and $R_q = 0.02$, $\mu = 12.0$. The resulting $\mathcal{N}_{in}(\text{eq})$ and T_b agreed with those predicted given the scaling exponents in (34) and (35) and the coefficients deduced from the previous four figures to within 20%.

c. Calculation of γ from the heton model

The success of our theory in predicting the correct exponents seen in the heton experiments gives us some confidence in the assumptions used in that theory; it is after all the use of these assumptions that allows us to gain some understanding of each model's behavior. We

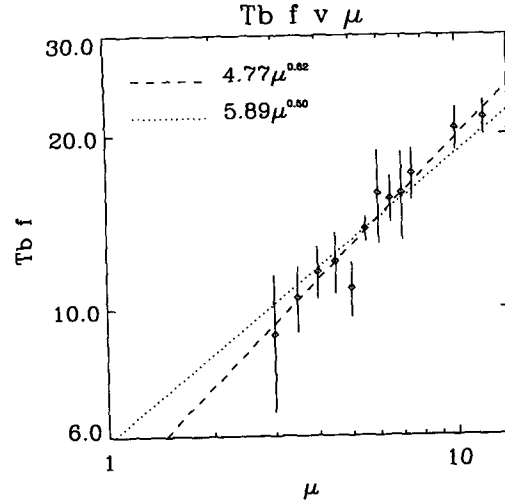


FIG. 11. Plot of T_{bf} vs μ at constant R_q . Shown are the data points, the best fit to these data points $T_{bf} = A1\mu^n$, and the best fit of $T_{bf} = A2\mu^{-1/2}$ to the data. $A1 = 4.77$, $n = 0.62 \pm 0.17$ and $A2 = 5.89$. Term n lies within one standard deviation of the predicted value.

now consider the constants of proportionality. Given the relation for $\mathcal{N}_{in}(\text{eq})$, Eq. (34), we can calculate γ_{2l} and hence γ_n and γ_s . The slope at constant μ (Fig. 12), $S_1 = \gamma_s \mu_0^{5/2}$, where $\mu_0 = 5.0$. The slope at constant R_q (Fig. 10), $S_2 = \gamma_s R_{q0}^{1/2}$, where $R_{q0} = 0.08$ so that

$$\gamma_{2l} = \frac{2^{1/4} S_p S_1}{\pi \mu_0^{5/2}} = \frac{2^{1/4} S_p S_2}{\pi R_{q0}^{1/2}}.$$

Inserting the numerical values ($S_1 = 91.3 \pm 6.1$, $S_2 = 0.48 \pm 0.05$, $S_p = 1.9$), we obtain $\gamma_{2l} = 1.17 \pm 0.08$

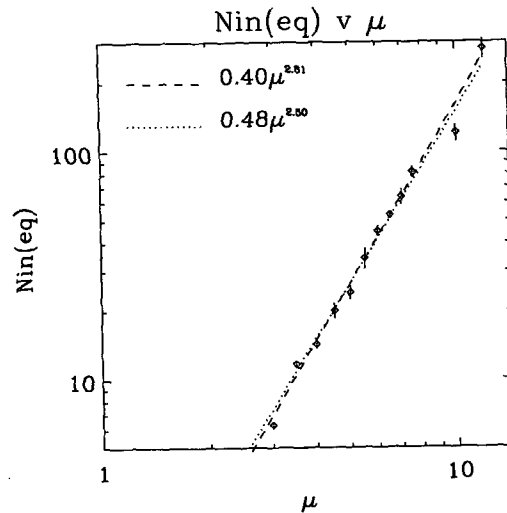


FIG. 12. Plot of \mathcal{N}_{in} vs μ at constant R_q . Shown are the data points, the best fit to these data points $\mathcal{N}_{in} = A1\mu^n$, and the best fit of $\mathcal{N}_{in} = A2\mu^{5/2}$ to the data. $A1 = 0.40$, $n = 2.61 \pm 0.10$, and $A2 = 0.48 \pm 0.05$; n is within two standard deviations of the predicted value.

or 1.22 ± 0.13 , reassuringly close in value, the difference between the two values being well within the estimated error. The closure parameter α relating the effective flux velocity with the geostrophic rim current is therefore deduced to be 0.25 ± 0.015 .

With regard to γ_n and γ_s , from Eq. (26), $\gamma_n = 1.56 \pm 0.14$ or 1.64 ± 0.24 and $\gamma_s = 1.77 \pm 0.07$ or 1.81 ± 0.13 . These should be compared with the values in VMJ, where $\gamma_s = 3.9 \pm 0.9$. While of a similar order of magnitude, the difference between the values of γ_s indicates a greater efficiency of the lateral fluxes in the heton model as compared to the numerical simulations and laboratory experiments studied in VMJ. This is especially evident in comparison of α' ($=\alpha/2^{3/2}$), which can be considered an efficiency parameter, where VMJ obtained $\alpha' = 0.008$ and we obtain $\alpha' = 0.088 \pm 0.004$, an order of magnitude greater. An explanation for this disparity in α' values may be found by comparing Figs. 4 and 5. Whereas the density anomaly in the heton model spreads out from the forcing region in a completely irrotational fashion, the density anomaly in the primitive equation simulations is swept around the forcing region as well as outward. In the quasigeostrophic formulation, the surface buoyancy forcing cannot generate a net vorticity (integrated in the vertical), while this constraint does not hold in the primitive equation case and a net cyclonic vorticity results. Hence for a given magnitude of eddy migration, the projection of the density transfer onto the direction away from the forcing region is greater in the quasigeostrophic case than in more complete formulations, and the effective flux velocity is therefore greater for the quasigeostrophic model.

6. Results of the heton model for elliptic forcing

Ocean convection observations indicate that the shape of the convecting region is often far from circular. For example, the MEDOC experiment (MEDOC 1970) observed a Mediterranean chimney much larger in east–west extent than north–south. Motivated by such observations, and as an example of the heton model's ready utility and economy, we performed a series of experiments to study the dependence of equilibrium conditions on the geometry of the forcing.

In order to predict the effect of shape we reconsider the equilibrium-state balance between surface forcing and lateral fluxes:

$$\int_{A_1} \frac{B_0 \rho_0}{g} dA = \int_h \oint_{l_1} u^* \Delta p dl dh, \quad (36)$$

where A_1 is now an arbitrarily shaped area, and l_1 is the perimeter length of that area. Then if we substitute for u^* relevant for the heton model to obtain the equilibrium density anomaly as before, we find a dependence on the shape:

$$\Delta \rho_{eq} = \frac{1}{2^{1/4} \alpha^{1/2}} \frac{\rho_0}{g} \left(\frac{NB_0}{h_{2l}} \right)^{1/2} (A_1/l_1)^{1/2}. \quad (37)$$

Hence we would predict forcing shapes with larger perimeters relative to area to result in lower equilibrium density anomalies due to the greater length over which the fluxes can occur.

We investigate whether this is the case by examining elliptic forcing regions. Choosing $R_q = 0.08$, we performed several series of experiments forced within an ellipse of area πab , where a and b are the two ellipse radii. For each series of experiments πab was fixed to correspond to the area of a circular vortex of radius $\mu = 3.0, 4.0, 5.0, 7.0, 10.0$. The ratio between the two ellipse axes a/b (Fig. 13) was reduced from 1.0 (a circle) to 0.5, 0.3, and 0.2. As the forcing becomes more elliptical, the circumference [approximately $l_1 = 2\pi\sqrt{(a^2 + b^2)/2}$] increases relative to area, and so an increase in the efficiency of the lateral fluxes might be expected, with a corresponding decrease in the final density anomaly and breakup time. However, contrary to the above prediction, our results showed no significant difference between the final density anomaly of the circular cases, and those for the equal-area elliptic regions (Fig. 14). This suggests that the circumference is not as important in controlling the behavior as one might expect, because instability development is modified by the altered shape. The elliptic shape imposes a mode 2 perturbation on the vortex, which interferes with the development of the preferred mode for baroclinic instability for the circular vortex of this area. As a result, fluxes do not occur across the whole of the circumference but principally at the regions of highest curvature of the ellipse (Fig. 15). Hence the effective length l_1 over which the fluxes are occurring is unchanged from the circular case. This suggests that, in applying parameterizations of the baroclinic instability lateral fluxes in the context of an isolated region of forcing, it is sufficient to know the area over

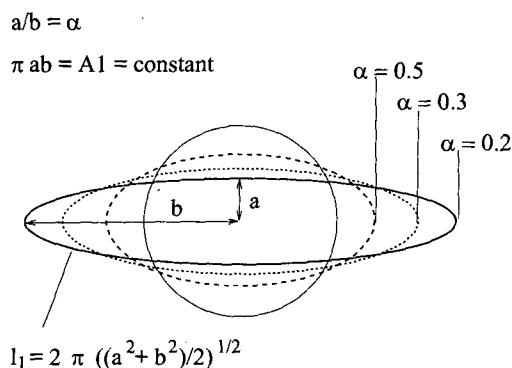


FIG. 13. A schematic comparing the areas and circumferences of circular and elliptic forcing regions. All are of equal area πab , where a and b are the lengths of the two axes, but $\alpha = a/b$ varies as in the numerical study described in the text.

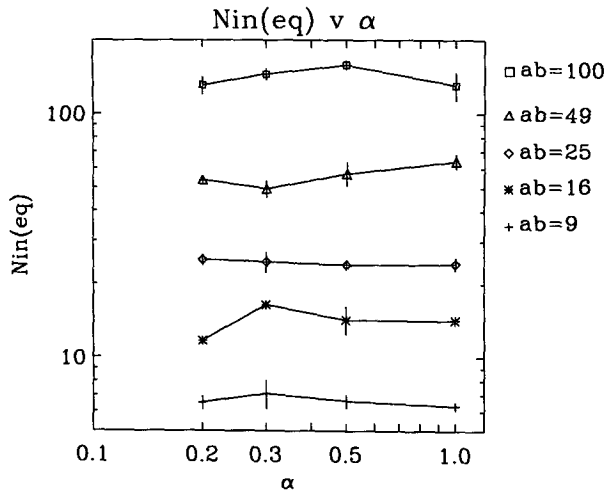


FIG. 14. Plot of $N_{in}(eq)$ vs μ at constant R_q for ellipses of different axis ratio α and different area πab ; $N_{in}(eq)$ shows negligible dependence on α .

which the forcing applies and not necessary to include the details of its spatial shape. However, this conclusion should be verified for more complex forcing shapes.

7. Discussion and conclusions

In this work we have investigated a quasi-equilibrium state of convection in a simple point-vortex heton model. This statistically steady state is established when the surface buoyancy loss is balanced by the lateral buoyancy fluxes achieved by the baroclinic instability associated with localized deep convection. We have compared the heton model results with those of other scenarios, for which other authors have investigated the equilibrium: the stratified model results have been verified by VMJ using supporting data from several studies (Ivey et al. 1995; Hufford et al. 1996, manuscript submitted to *J. Geophys. Res.*), and the neutral scenario results have been verified by Brickman (1995) and Narimousa (1996, manuscript submitted to *J. Geophys. Res.*). We have shown that the properties of the equilibrium state in the heton model can be explained using two assumptions: 1) at equilibrium the transfer of heat by geostrophic eddies arising through baroclinic instability balances the surface buoyancy forcing and 2) the root-mean-square velocity of material across the chimney boundary is proportional to the magnitude of the rim current around the chimney. The importance of this advective balance is confirmed by the successful application of an identical parameterization of the lateral fluxes in this model as in other scenarios, despite the model's very different quasigeostrophic dynamics. The potential vorticity parameterization of convection inherent in the heton model is also corroborated by the agreement between the heton results and those of other

scenarios. The conclusion that the fluxes are independent of molecular parameters or subgrid-scale parameterizations is confirmed by the use of an inviscid model. Objective comparison between the heton model results and those of other scenarios is only possible given the unified formulation we have described, since as we have shown the details of the scaling ultimately depend on the depth over which convective forcing applies and the determination of deformation radius. In particular the quasigeostrophic model keeps the deformation radius fixed and dependent on the initial stratification. Hence, although an analogous scaling behavior and identical mechanism for establishment of an equilibrium apply, results from a quasigeostrophic model cannot be applied blindly to the real ocean. Rather they should be used to provide an understanding of the underlying processes. This formulation can be extended to apply to many other convection scenarios, including, for example, nonuniform stratification or varying buoyancy fluxes.

In the simulations described in this paper the localization of the convection has been artificially imposed, as in most of the studies of localized convection to date. However, in many areas where open-ocean deep convection occurs, it is likely that the localization is a result of weakened stratification associated with an ambient cyclonic flow (Swallow and Caston 1973). This pre-existing circulation may have a significant influence on the ability of baroclinic instability to provide a sufficiently large lateral heat flux (Legg and Marshall: The influence of ambient flow on the spreading of convected water masses, in preparation). The simplified dynamics of the heton model allows circumstances such as these to be identified analytically. In addition, ambient circulation will play a significant role in determining how the overturned fluid mixes with its surroundings, thus affecting the characteristics of the new water mass.

This study has assumed that convection occurs in a localized region located in an effectively infinite ocean, allowing all mixed water to escape. If the ocean basin is of finite extent, the flux of fluid out of the convecting region by the baroclinic instability will not be sufficient to prevent further deepening and cooling of the overturned water mass since fluid may be "processed" by the convecting region several times. The finite size of the basin may not be important in the real ocean, where the timescale for processing all the water of the basin is probably greater than the seasonal scale of the forcing; however, in laboratory and numerical experiments finite domain size has a significant influence.

Since these results have indicated the importance of the radius of the forced region, further important questions remain concerning the spatial distribution of the buoyancy loss. Most studies of localized convection performed to date have assumed a top hat form of the buoyancy forcing, constant over a circular region and

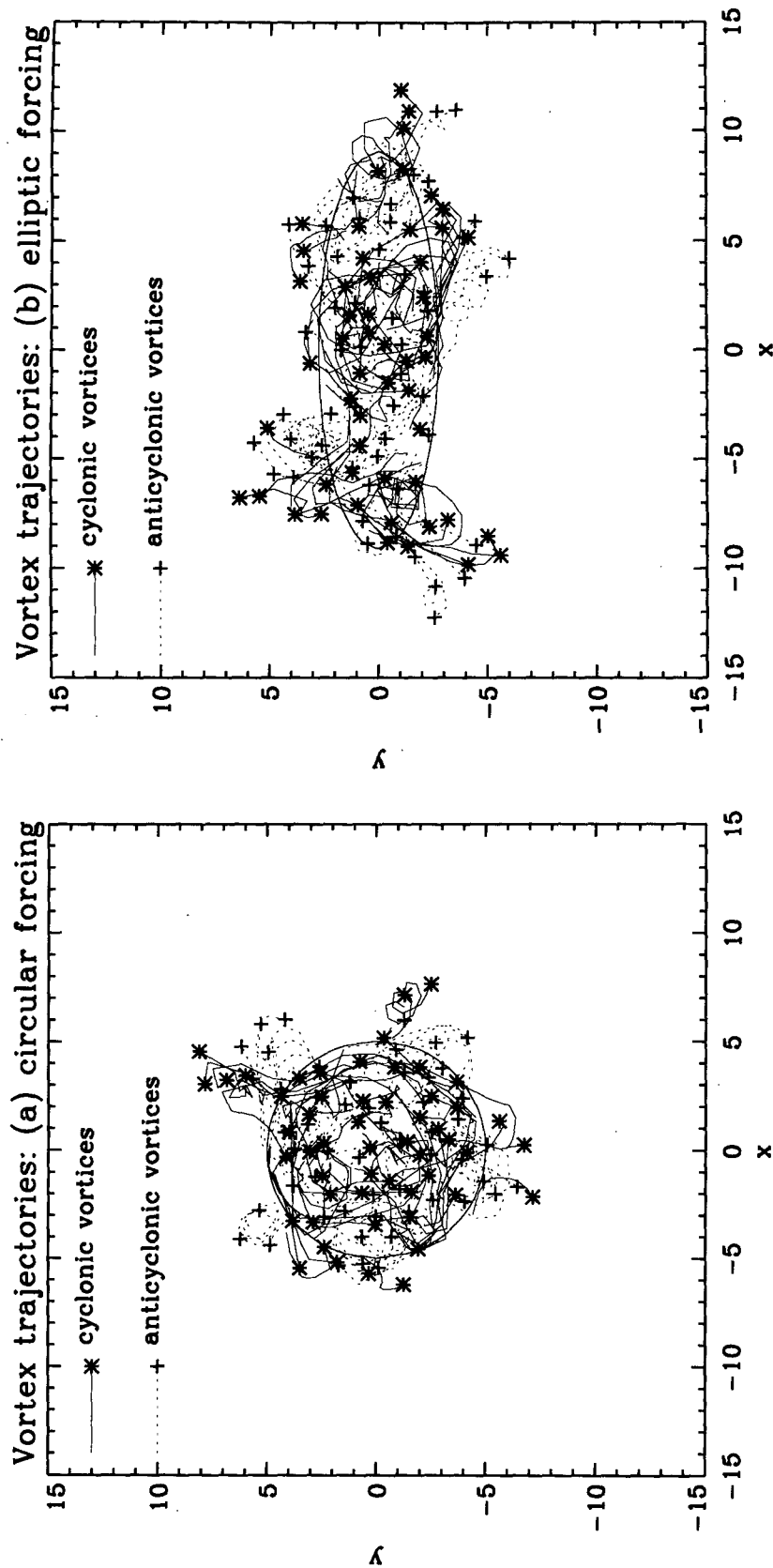


FIG. 15. Vortex trajectories for forcing over an elliptic area (outlined by a thin solid line) with an area $25\mu^2$ and axis ratio (a) $\alpha = 1.0$ (circular forcing) and (b) $\alpha = 0.3$. Vortex trajectories are shown for a time period of $\Delta t = 7.2/f$, beginning from a time $t_0 = 16.8/f$ after the onset of cooling. In the circular case, a mode 4 instability distributes the sites where vortices (representing denser fluid) are breaking out evenly around the perimeter, while in the elliptic forcing case, vortices are breaking out principally from the two lobes of the ellipse.

negligible outside. Convection is usually forced by surface buoyancy loss over an area that is far from circular, with the intensity of the buoyancy loss showing a more gradual decrease from its maximum. Our preliminary investigations into elliptic-shaped forcing show surprisingly little dependence of the density anomaly on the shape of the forcing region; the instability is modified by the shape perturbation, compensating for the lengthened perimeter of the forcing region, and no increase in lateral fluxes therefore occurs. However, it is not clear that this will be the case for all forcing topologies. If convection occurs simultaneously at several locations, there may be interaction and transfer of fluid between the different regions. The heton model is ideally suited to address these questions in future work since its economy offers a ready means of scouting parameter space in preparation for more costly explicit computational and laboratory studies. We emphasize that the heton model is best suited for examining questions determined by horizontal structure (such as the study of forcing shape described earlier) since it includes a minimal vertical representation. In this respect it provides a useful complement to the two-dimensional model of Visbeck et al. (1996b), which assumes some symmetry in one of the horizontal directions (i.e., flow and density independent of zonal or azimuthal direction) but can resolve structure in the vertical. A limited number of high-resolution numerical studies will always be a necessary follow up to verify any interesting results in the context of more complete representations of the three-dimensional structure.

In conclusion, the idealizations of the heton model—its inviscid nature, and simplified quasigeostrophic dynamics—allow us to isolate the advective fluxes associated with baroclinic instability alone, as distinct from diffusive effects and vertical mixing, which may be present in other models and laboratory experiments. The presence of an equilibrium in this model, with a dependence on imposed parameters which is easily related to that found by other researchers in more complex scenarios, confirms that the dominant process is indeed advective and controlled by baroclinic instability.

Acknowledgments. SL and MV are supported by the National Oceanic and Atmospheric Administration postdoctoral program in Climate and Global Change, administered by the Universities Corporation for Atmospheric Research. Part of this work was carried out while SL was a postdoctoral research associate at the Joint Institute for Laboratory Astrophysics, University of Colorado, and funded by the NSF High Performance Computing and Communications Grant ECS9217394. HJ is supported by the MAST II Program of the EC as part of MERMAIDS. We would like to thank John Marshall, Alistair Adcroft, and two anonymous reviewers for comments on an earlier version of the manuscript.

APPENDIX

The Heton Model Equations

The equations governing the development of the convection patch in the heton model are

$$\frac{Dq_1}{Dt} = -\frac{Dq_2}{Dt} = \frac{-B_0 f}{h_{2l}^2 N^2} \mathcal{H}(\zeta - r) \quad (\text{A1a})$$

$$s \frac{D\mathcal{N}}{Dt} = \int_{A_1} \frac{Dq_1}{Dt} dA = - \int_{A_1} \frac{Dq_2}{Dt} dA \quad (\text{A1b})$$

$$\nabla^2 \psi_1 - \frac{1}{2\lambda^2} (\psi_1 - \psi_2) = \sum_{i=1, \mathcal{N}} s \delta(\zeta - r_{1,i}) \quad (\text{A1c})$$

$$\nabla^2 \psi_2 - \frac{1}{2\lambda^2} (\psi_2 - \psi_1) = \sum_{i=1, \mathcal{N}} -s \delta(\zeta - r_{2,i}), \quad (\text{A1d})$$

where $\mathcal{H}(x)$ is the Heavyside function, $\mathcal{H}(x) = 1, x < 0$, $\mathcal{H}(x) = 0, x > 0$; $\lambda = Nh_{2l}/(\sqrt{2}f)$, the deformation radius; ψ is the streamfunction; q is the quasigeostrophic potential vorticity; \mathcal{N} is the total number of baroclinic point vortices (hetons); B_0 is the surface buoyancy forcing; h_{2l} is the depth of the layer; r and $A_1 = \pi r^2$ are the radius and area of the forcing region; s and $-s$ are the strengths of a point vortex in the upper and lower layers, respectively; and N is the Brunt–Väisälä frequency. The subscripts 1, 2 refer to the upper and lower layers, respectively. In Eqs. (A1) ζ is the position coordinate and $r_{n,i}$ is the position coordinate of the i th vortex in the n th layer. In the two-layer system N is defined by $N^2 = g \Delta \rho_{1,2} / (h_{2l} \rho_0)$, where $\Delta \rho_{1,2}$ is the density difference between the layers.

We nondimensionalized these equations using $1/f$ and λ as the temporal and spatial scales:

$$t = \frac{t^*}{f} \quad (\text{A2a})$$

$$L = L^* \lambda. \quad (\text{A2b})$$

Then the equation set (A1) becomes, where all parameters are now nondimensional,

$$\frac{Dq_1}{Dt} = -\frac{Dq_2}{Dt} = R_q \mathcal{H}(\zeta - \mu) \quad (\text{A3a})$$

$$\frac{D\mathcal{N}}{Dt} = \frac{R_q}{S_p} \mu^2 \pi \quad (\text{A3b})$$

$$\nabla^2 \psi_1 - \frac{1}{2} (\psi_1 - \psi_2) = \sum_{i, \mathcal{N}} S_p \delta(\zeta - r_{1,i}) \quad (\text{A3c})$$

$$\nabla^2 \psi_2 - \frac{1}{2} (\psi_2 - \psi_1) = \sum_{i, \mathcal{N}} -S_p \delta(\zeta - r_{2,i}), \quad (\text{A3d})$$

where there are three nondimensional constants:

$$R_q = \frac{B_0}{h_{2l}^2 N^2 f} \quad (\text{A4a})$$

$$S_p = \frac{s}{\lambda^2 f} \quad (\text{A4b})$$

$$\mu = \frac{r}{\lambda} = \frac{\sqrt{2}rf}{Nh_{2l}} \quad (\text{A4c})$$

The equation set in its nondimensional form (A3) is integrated forward using a fourth-order Runge–Kutta time-differencing scheme to find the evolution of the point-vortex positions, and hence the behavior of the convective patch.

REFERENCES

- Brickman, D., 1995: Heat flux partitioning in open-ocean convection. *J. Phys. Oceanogr.*, **25**, 2609–2623.
- Charney, J. G., 1947: The dynamics of long waves in a baroclinic westerly current. *J. Meteor.*, **4**, 135–163.
- Coates, M. J., G. N. Ivey, and J. R. Taylor, 1995: Unsteady, turbulent convection into a rotating, linearly stratified fluid: Modeling deep ocean convection. *J. Phys. Oceanogr.*, **25**, 3032–3050.
- Eady, E. T., 1949: Long waves and cyclone waves. *Tellus*, **1**, 33–52.
- Fernando, H. J. S., R.-R. Chen, and D. L. Boyer, 1991: Effects of rotation on convective turbulence. *J. Fluid Mech.*, **228**, 513–547.
- Gascard, J.-C., 1978: Mediterranean deep water formation, baroclinic instability and oceanic eddies. *Oceanol. Acta*, **1**, 315–330.
- Griffiths, R. W., and E. J. Hopfinger, 1984: The structure of meso-scale turbulence and horizontal spreading at ocean fronts. *Deep-Sea Res.*, **31**, 245–269.
- Helfrich, K. R., and U. Send, 1988: Finite-amplitude evolution of two-layer geostrophic vortices. *J. Fluid Mech.*, **197**, 331–348.
- Hogg, N. G., and H. M. Stommel, 1985: Hetonic explosions: The breakup and spread of warm pools as explained by baroclinic point vortices. *J. Atmos. Sci.*, **42**, 1465–1476.
- Ivey, G. N., J. R. Taylor, and M. J. Coates, 1995: Convectively driven mixed layer growth in a rotating, stratified fluid. *Deep-Sea Res.*, **42**, 331–349.
- Jones, H., and J. Marshall, 1993: Convection with rotation in a neutral ocean: A study of open-ocean deep convection. *J. Phys. Oceanogr.*, **23**, 1009–1039.
- Killworth, P. D., 1983: Deep convection in the world ocean. *Rev. Geophys. Space Phys.*, **21**, 1–26.
- Legg, S., and J. Marshall, 1993: A heton model of the spreading phase of open-ocean deep convection. *J. Phys. Oceanogr.*, **23**, 1040–1056.
- Madeo, G., M. Chartier, P. Delecluse, and M. Crepon, 1991: A three-dimensional numerical study of deep water formation in the northwestern Mediterranean sea. *J. Phys. Oceanogr.*, **21**, 1349–1371.
- Maxworthy, T., and S. Narimousa, 1994: Unsteady, turbulent convection into a homogeneous, rotating fluid, with oceanographic applications. *J. Phys. Oceanogr.*, **24**, 865–887.
- MEDOC group, 1970: Observation of formation of deep water in the Mediterranean sea. *Nature*, **227**, 1037–1040.
- Pedlosky, J., 1985: The instability of continuous heton clouds. *J. Atmos. Sci.*, **42**, 1477–1486.
- Send, U., and J. Marshall, 1995: Integral effects of deep convection. *J. Phys. Oceanogr.*, **25**, 855–872.
- Stone, P., 1972: A simplified radiative-dynamical model for the static stability of rotating atmospheres. *J. Atmos. Sci.*, **29**, 405–418.
- Swallow, J. C., and G. F. Caston, 1973: The preconditioning phase of Medoc 1969—I. Observations. *Deep-Sea Res.*, **20**, 429–448.
- Turner, J. S., 1973: *Buoyancy Effects in Fluids*. Cambridge University Press, 367 pp.
- Visbeck, M., J. Marshall, and H. Jones, 1996a: Dynamics of isolated convective regions in the ocean. *J. Phys. Oceanogr.*, **26**, 1721–1734.
- , —, T. Haine, and M. Spall, 1996b: On the specification of eddy transfer coefficients in coarse resolution ocean circulation models. *J. Phys. Oceanogr.*, **26**, in press.